Numerical Solution of Radiative Flowfield on the Nose Region of Blunt Bodies

Shen Jian-wei and Qu Zhang-hua
Changsha Institute of Technology
Changsha Hunan, China

Abstract

The radiative viscous flow over hypersonic blunt bodies is calculated numerically. Chemical nonequilibrium and equilibrium are considered with viscous shock layer equations. Both line and continuum radiation models are employed. One-dimensional planar medium assumption is used to deal with radiative transport so that the spatial marching technique is available in numerical calculation. The numerical results show that the convective heating transfer rate prevails as the reentry velocity lower than 7.6 km / sec at high altitude, the radiative heating transfer rate increases with the increase of freestream velocity and density.

Nomenclature

B_ν	Planck spectral radiative intensity
C_i	mass fraction of species i, ρ_i^* / ρ^*
Cp	specific heat at constant pressure, Cp^* / Cp_∞^*
$\overline{F}$	radiative flux
h	static enthalpy, h^* / U_∞^{*2}
h_i	static enthalpy of species i, h_i^* / U_∞^{*2}
h_1, h_3	shape factors for a general orthogonal coordinate system, $h_1 = 1 + \kappa y$, $h_3 = r + y\cos\varphi$
I_ν	radiative intensity
k	thermal conductivity
Le	Lewis number
M_i	molecular weight of species i
$\overline{M}$	average molecular weight of mixture
ns	the number of species
p	pressure, $p^* / (\rho_\infty^* U_\infty^{*2})$
Pr	Prandtl number
q_w	heating transfer rate, $q_w^* / (\rho_\infty^* U_\infty^{*3})$
R_n^*	nose radius
R	universal gas constant
T	temperature, T^* / T_{ref}^*
T_{ref}^*	reference temperature, $U_\infty^{*2} / Cp_\infty^*$
U_∞^*	freestream velocity
u	velocity component parallel to the body surface, u / U_∞^*
v	velocity component normal to the body surface, v / U_∞^*
w	local change rate of species due to chemical reactions
x, y	body – oriented coordinate system, x^* / R_n^*, y^* / R_n^*
α_ν	volumetric absorption coefficient
β	mesh refinement parameter
ε	Reynolds number parameter, $\varepsilon = [\mu_{ref}^* / (\rho_\infty^* U_\infty^* R_n^*)]^{1/2}$
δ	shock standoff distance, δ^* / R_n^*
ξ, η	normalized coordinates
κ	wall curvature, $\kappa^* R_n^*$
μ	viscosity of mixture, μ^* / μ_{ref}^*
ρ	density, ρ^* / ρ_∞^*
σ	shock angle
φ	body angle

Subscripts

i	ith species
ref	reference condition
s	quantities immediately behind the shock
w	body surface quantities
∞	freestream condition

Superscript

*	dimensional variable

I Introduction

As the space vehicles reenter the atmosphere at hypersonic speed, especially for blunt bodies with large nose radius, dissociation and ionization take place in the shock layer since the temperature is much high. Radiation transport is also an important phenomena of the flowfield, and it has the effect on the surface heating transfer rate. The radiative flowfield of reentry vehicle can be analyzed with the viscous shock–layer(VSL)

This work was supported through National Natural Science Foundation of China

method, which is an approximation of Navier–Stokes equations for viscous flow. The VSL method maintains the advantage of Boundary Layer method and avoids the trouble caused by determining the outer edge of boundary layer. The bow shock is taken as outer edge of the flow, and a set of uniform governing equations is used in the whole region from the body to the shock. The governing equations can be solved with spatial marching technique so that less computing time is needed than that of the time–dependent method.

Based on the viscous shock–layer model, nonequilibrium and equilibrium chemistry, as well as radiation transport are considered for the real gas effects. As the radiation is considered, the energy equation is in an integro–differential form and the radiation flux is strong nonlinear coupled with temperature, thus it is more difficult to get the temperature profiles from solving the energy equation. The radiative intensity in all directions must be taken into account as the angular integration is carried out for the radiation flux, which makes the properties of the flowfield at one station depending on the downstream region. For nonequilibrium flow, the assumption of frozen–shock condition is overly estimated the temperature immediately behind the shock, and it needs to be improved as the radiation is considered with one temperature model. In order to obtain the solution of radiative reentry flowfield with spatial marching technique, one–dimensional planar geometry assumption is employed for radiative transport. The radiative flux divergence in energy equation is treated as a source term, and it is relaxed to get temperature profiles by iteration.

II Analysis

Governing Equations

Viscous shock–layer equations coupling with radiation contain a term of radiative flux divergence in energy equation, and a radiative transport equation is added to determine the radiative intensity. For nonequilibrium flow, the species continuity equations are also needed. In the axisymmetric body oriented coordinate system (see Fig.1), the governing equations are as follows:

global continuity equation

$$\frac{\partial}{\partial x}(h_3\rho u)+\frac{\partial}{\partial y}(h_1h_3\rho v)=0 \qquad (1)$$

x–momentum equation

$$\rho u\frac{\partial u}{h_1\partial x}+\rho v\frac{\partial u}{\partial y}+\frac{\kappa\rho uv}{h_1}=-\frac{\partial p}{h_1\partial x}$$
$$+\frac{\varepsilon^2}{h_1^2h_3}\frac{\partial}{\partial y}[\mu h_1^2h_3(\frac{\partial u}{\partial y}-\frac{\kappa u}{h_1})] \qquad (2)$$

y–momentum equation

$$\rho u\frac{\partial v}{h_1\partial x}+\rho v\frac{\partial v}{\partial y}-\frac{\kappa\rho u^2}{h_1}=-\frac{\partial p}{\partial y} \qquad (3)$$

energy equation

$$\rho uCp\frac{\partial T}{h_1\partial x}+\rho vCp\frac{\partial T}{\partial y}-u\frac{\partial p}{h_1\partial x}-v\frac{\partial p}{\partial y}$$
$$=\frac{\varepsilon^2}{h_1h_3}\frac{\partial}{\partial y}(kh_1h_3\frac{\partial T}{\partial y})+\varepsilon^2\mu(\frac{\partial u}{\partial y}-\frac{\kappa u}{h_1})^2$$
$$+\varepsilon^2\sum_{i=1}^{ns}\frac{\mu Le}{Pr}\frac{\partial C_i}{\partial y}Cp_i\frac{\partial T}{\partial y}-\varepsilon^2\sum_{i=1}^{ns}h_iw_i+Q_R \qquad (4)$$

for chemical nonequilibrium flow

$$\rho u\frac{\partial h}{h_1\partial x}+\rho v\frac{\partial h}{\partial y}-u\frac{\partial p}{h_1\partial x}-v\frac{\partial p}{\partial y}=$$
$$\frac{\varepsilon^2}{h_1h_3}\frac{\partial}{\partial y}(kh_1h_3\frac{\partial T}{\partial y})+\varepsilon^2\mu(\frac{\partial u}{\partial y}-\frac{\kappa u}{h_1})^2$$
$$+\varepsilon^2\frac{\partial}{\partial y}[\sum_{i=1}^{ns}h_i\frac{\mu Le}{Pr}\frac{\partial C_i}{\partial y}]+Q_R \qquad (5)$$

for chemical equilibrium flow

species equation

$$\rho u\frac{\partial C_i}{h_1\partial x}+\rho v\frac{\partial C_i}{\partial y}=w_i$$
$$+\frac{\varepsilon^2}{h_1h_3}\frac{\partial}{\partial y}(h_1h_3\frac{\mu Le}{Pr}\frac{\partial C_i}{\partial y}) \qquad i=1,\ldots,ns \qquad (6)$$

for chemical nonequilibrium flow

$$C_i=C_i(p,h) \qquad (7)$$

for chemical equilibrium flow

state equation

$$p=\frac{\rho RT}{\bar{M}Cp_\infty^*} \qquad (8)$$

for chemical nonequilibrium flow

$$\rho=\rho(p,h) \qquad (9)$$

for equilibrium flow

radiation transport equation

$$\nabla I_\nu\cdot\bar{l}=\alpha_\nu[B_\nu-I_\nu] \qquad (10)$$

where $\bar{l}$ is the unit vector along optical path.

Radiative Transport

Radiative flux at one point in the shock layer is

$$\bar{F}=\int_0^\infty\int_0^{4\pi}I_\nu\bar{l}\,d\Omega d\nu \qquad (11)$$

where $d\Omega$ is solid angle about the unit vector $\bar{l}$, ν is frequency.

The radiative flux divergence appeared in energy equation is

$$Q_R=-\nabla\cdot\bar{F} \qquad (12)$$

Since the shock layer is thin at the hypersonic reentry velocity, it is assumed that the gradient in normal direction of body surface is much larger than that in tangent direction, thus the radiation transport equation can be expressed as follows:

$$\cos\psi \frac{\partial I_\nu}{\partial y} = \alpha_\nu (B_\nu - I_\nu) \quad (13)$$

where ψ is the angle between radiative flux vector and the normal direction from the body surface.

The radiative flux divergence Q_R in energy equation can be expressed as:

$$Q_R = -\nabla \cdot \vec{F} = \int_0^\infty \int_0^{4\pi} \alpha_\nu (I_\nu - B_\nu) d\Omega d\nu \quad (14)$$

the range of integration for $d\Omega$ in equation (14) is carried out through 4π solid angle, thus the radiative intensity coming from downstream region has the effect on the upstream properties. In order to make the spatial marching technique available, the angular integration in equation (14) is carried out using the forward–reverse approximation, that is, the intensity is divided into two angular groups: those rays passing through the plane of symmetry in the positive direction from wall to shock and those rays passing in the negative direction from shock to wall.The forward–reverse approximation represents all rays in the positive direction by a single ray I_ν^+ with an average direction cosine $1/f$, and all rays in the negative direction by a single ray I_ν^-, also with an average direction cosine $1/f$, see Fig.2

Solving equation (13) with the assumption of one–dimentional planar radiation transport model, we have

$$I_\nu^+(y) = \int_0^y \alpha_\nu(y') B_\nu(y') \exp[-\frac{1}{f}\int_{y'}^{y} \alpha_\nu(y'')dy''] \frac{1}{f} dy' \quad (15)$$

$$I_\nu^-(y) = \int_y^\delta \alpha_\nu(y') B_\nu(y') \exp[-\frac{1}{f}\int_{y}^{y'} \alpha_\nu(y'')dy''] \frac{1}{f} dy' \quad (16)$$

The absorption coefficient α_ν is divided into two parts

$$\alpha_\nu = \alpha_\nu^C + \alpha_\nu^L \quad (17)$$

where α_ν^C and α_ν^L corresponds to continuum and line contribution of the radiation.

Introduce emissive function $E(y',y)$ and equivalent width variable $W_i(y',y)$ as follows: [15]

$$E(y',y) = 1 - \exp[-\frac{1}{f}\int_{y'}^{y} \alpha_\nu^C(y'')dy''] \quad (18)$$

$$W_i(y',y) = \exp[-\frac{1}{f}\int_{y'}^{y}\alpha_\nu^C(y'')dy'']\int_{\Delta\nu}\{1 - \exp[-\frac{1}{f}\int_{y'}^{y}\alpha_\nu^L(y'')dy'']\}d\nu \quad (19)$$

Radiative flux F can be expressed in two parts corresponds to α_ν^C and α_ν^L as follows:

$$F = F^C + F^L \quad (20)$$

where:

$$F^C = \pi\int_0^\infty [\int_0^{B(0,y)} B_\nu dE(y',y) - \int_0^{B(y,\delta)} B_\nu dE(y,y')]d\nu \quad (21)$$

$$F^L = \pi\sum_i [\int_0^{W_i(0,y)} B_\nu dW_i(y',y) - \int_0^{W_i(y,\delta)} B_\nu dW_i(y,y')] \quad (22)$$

The radiative flux divergence Q_R in energy equation can be expressed as:

$$Q_R = Q^{CC} + Q^{CL} + Q^{LC} + Q^{LL} \quad (23)$$

where:

$$Q^{CC} = 2\pi\int_0^\infty \alpha^C(y)\{\int_0^{B_\nu(0,y)} B_\nu(y')dE_\nu(y',y) + \int_0^{B_\nu(y,\delta)} B_\nu(y')dE_\nu(y,y') - 2B_\nu(y)\}d\nu \quad (24)$$

$$Q^{CL} = 2\pi\sum_i\{\int_0^{B_\nu(0,y)} B_{\nu i}(y')[S_i(y) - A_i(y',y)]dE_\nu(y',y) + \int_0^{B_\nu(y,\delta)} B_{\nu i}(y')[S_i(y) - A_i(y,y')]dE_\nu(y,y')\} \quad (25)$$

$$Q^{LC} = 2\pi\sum_i \alpha_i^C(y)\{\int_0^{W_i(0,y)} B_{\nu i}(y')dW_i(y',y) + \int_0^{W_i(y,\delta)} B_{\nu i}(y')dW_i(y,y')\} \quad (26)$$

$$Q^{LL} = 2\pi\sum_i\{\int_0^{A_i(0,y)} B_{\nu i}(y') \exp[-\frac{1}{f}\int_{y'}^{y}\alpha_\nu^C(y'')dy'']dA_i(y',y) + \int_0^{A_i(y,\delta)} B_{\nu i}(y')\exp[-\frac{1}{f}\int_{y}^{y'}\alpha_\nu^C(y'')dy'']dA_i(y,y') - 2B_{\nu i}(y)S_i(y)\} \quad (27)$$

$$A_i(y',y) = \int_{\Delta\nu}\alpha_{\nu i}^L(y)\{1 - \exp[-\frac{1}{f}\int_{y'}^{y}\alpha_{\nu i}^L(y'')dy'']\}d\nu \quad (28)$$

$$S_i(y) = \int_0^\infty \alpha_{\nu i}^L(y)d\nu \quad (29)$$

The volumetric absorption coefficient α^C and α^L are treated the same as in reference [15].

Boundary Conditions

Boundary Conditions at the Bow Shock

The Rankine–Hugoniot equations are used to obtain the shock boundary conditions. Non–dimentional Rankine–Hugoniot equations written in body oriented coordinate (see figure 1) are as follows:

$$u_s = \cos\sigma\cos(\sigma - \varphi) + \bar{\rho}\sin\sigma\sin(\sigma - \varphi) \quad (30)$$

$$v_s = \cos\sigma\sin(\sigma - \varphi) - \bar{\rho}\sin\sigma\cos(\sigma - \varphi) \quad (31)$$

$$p_s = (1 - \bar{\rho})\sin^2\sigma + p_\infty \quad (32)$$

$$h_s = 0.5 * (1 - \bar{\rho}^2)\sin^2\sigma + h_\infty \quad (33)$$

where $\bar{\rho} = 1/\rho_s$

Species mass fractions at the shock are:

$$C_{is} = C_i(p_s, h_s) \quad (34)$$

The specific intensity condition is

$$I_\nu^- = 0 \tag{35}$$

which means that the specific intensity coming through the shock towards the body is specified as zero.

Boundary Conditions at the Wall

The wall is treated as no–slip and no injection boundary.

$$y = 0 \quad u = 0, \quad v = 0, \quad T = T_w \tag{36}$$

$C_i = C_{iw}$ full catalytic wall for nonequilibrium flow

$C_i = C_i(p_w, h_w)$ for equilibrium flow

the specific intensity at the wall is

$$I_\nu^+ = 0 \tag{37}$$

which means that the wall is full absorption surface.

Thermodynamic and Transport Properties

The enthalpy and frozen specific heat of species i at constant pressure are got from the datalist given by Browne [7] [8] . the species viscosity and heat conductivity are given by curve fit relations as Blottner [9] .

The approximate viscosity and conductivity of the gas mixture are given by:

$$\mu = \sum_{i=1}^{ns} \frac{X_i \mu_i}{\sum_{j=1}^{ns} X_j \Phi_{ij}} \tag{38}$$

$$k = \sum_{i=1}^{ns} \frac{X_i k_i}{\sum_{j=1}^{ns} X_j \Phi_{ij}} \tag{39}$$

where $X_i = C_i \frac{\overline{M}}{M_i}$

$$\Phi_{ij} = [\, 1 + (\frac{\mu_i}{\mu_j})^{\frac{1}{2}} (\frac{M_j}{M_i})^{\frac{1}{4}}]^2 \,/\, [\, 8(1 + \frac{M_i}{M_j})]^{\frac{1}{2}} \tag{40}$$

III Numerical Calculation

The following coordinate transformation is used in numerical calculation

$$\xi = x \tag{41}$$

$$\eta = 1 - \frac{1}{\ln(\frac{\beta + 1}{\beta - 1})} \ln(\frac{\beta - y / y_s + 1}{\beta + y / y_s - 1}) \tag{42}$$

The flowfield between the body surface and the bow shock becomes a regular region with this transformation, thus the square grids can be used and more grids are arranged near the body surface in physical space to be suited for the large gradient of the flow properties at high Reynolds number.

The physical properties of the flowfield are normalized by the values at the bow shock with the exception of normal velocity and species concentrations to avoid taking zero as denominator.

Numerical calculation starts from the stagnation line, then marches downstream along the body surface. At the stagnation line, the physical properties and geometric parameters are expanded as a series of ξ , so that the governing equations become a set of ordinary differential equations with a souce term of radiative flux divergence in energy equation, and they are solved with finite–difference method. The results of stagnation line are used as the initial value of spatial marching.

The tangential momentum equation, energy equation and species continuity equation can be expressed as standard parabolic equation, and they are solved with Stoimachic algorithm. As the energy equation and species equations are written in the standard parabolic form for nonequilibrium flow, the formation terms are dealed with quasi–linearization. the radiative flux divergence in energy equation is relaxed to get the temperature profiles.the global continuity equation and normal momentum equation are solved in a coupled way [10] . The shock stand–off distance is determined by integration of the global continuity equation.

IV Results and Discussion

Hypersonic flows over reentry blunt bodies are calculated using spatial marching finite–difference method. The flight altitudes are from 65km to 90km.

Fig.3 is the comparison of temperature profiles, both radiation and no radiation are presented. The grid stretch method is compared with that of Dorodnitzn transformation [11] , the former is more adequate for large Reynolds number and low wall temperature, and it is more suitable for marching downstream calculation from the stagnation streamline. The results show that the temperature profiles agree quite well with each other, which checked the equilibrium code of this study and proved that a reasonable initial value can be applied for marching downstream from the stagnation streamline. It also shows that the temperature behind the shock is reduced due to the emission as the radiation is coupled.

Fig.4 is the comparison of heating transfer coefficient with Engle's [11] . It shows that the radiative heating increases rapidly with the increase of freestream velocity just as that in Ref.11. The small difference between the two results is due to the different numerical methods.

Fig.5 is the results comparison with Gupta's (Ref.12). The freestream conditions are taken from the trajectory points of Fire II [14]. It shows that the agreement of the two results is quite well.

Figs.6–7 are the results of marching downstream. Fig.6 and Fig.7 are convective and radiative heating rate distribution, respectively. the freestream velocities are from 7 km / sec to 15 km / sec, the altitude is 65 km. The results show that the radiative heating is greatly affected by freestream velocity, it may increase several orders of magnitude as the freestream velocity increases only by two times. The change of convective heating is relatively small. This is because the radiative heating depends on the temperature itself, but the convective heating depends on the gradient of temperature.

Figs.8–10 are the results of different nose radius. They show that the radiative heating increases with nose radius increasing, but, on the contrary, the convective heating is reduced.

Fig.11 is the results of radiative heating at different altitude. It shows that the radiative heating increases about 3 orders of magnitude from 83 km to 40 km. In fact, the lower the altitude, the greater the density. The species number density of the air is larger at the low altitude, thus the radiative flux increases with the decrease of the altitude.

Fig.12 is the temperature profiles at different downstream stations. It shows that the highest temperature in the nose region is at the shock, but in far downstream region, the highest temperature is near the wall, which shows the viscous effects of the hypersonic flow.

Figs.13–18 are the results of nonequilibrium flow. Seven species are included in nonequilibrium chemistry(N_2, O_2, N, O, NO, NO^+, e^-). the chemical reactions are assumed to proceed at finite rate.

Figs.13–16 are the results of convective and radiative heating transfer, respectively. They are compared with those from Gupta [12] at the stagnation streamline, and they show that both convective and radiative heating transfer agree well with Ref.12. As the altitude is above 81km, the convective heating is much larger than radiative heating at the velocity of 9.89 km / sec.

Figs.17–18 are the results of heating transfer at the altitude of 90km. The comparison with Moss' [13] results shows that the results of VSL method are agree well with that of DSMC method.

Concluding Remarks

It can be concluded from the study of this paper that the radiating viscous shock layer can be calculated using spatial marching finite–difference method as a planar radiative transport model is employed. The energy equation in integro–differential form can be solved as a partial differential equation with the radiative flux divergence term relaxed by iteration.

The radiative heating transfer at the body surface is neglectable as the reentry velocity is lower than 7.6km / sec, and it increases rapidly with the increase of freestream velocity, density and nose radius. As the freestream velocity is 15 km / sec, the radiative heating is larger than the convective heating.

References

[1] Gupta,R.N., Lee,K.P., Moss,J.N., Zoby,E.V. and Tiwari,S.N., "Viscous Shock–Layer Analysis of Hypersonic Flows over Long Slender Bodies," AIAA Paper No.87–2487, 1987.

[2] Swaminathan,S., Kim,M.D. and Lewis,C.H., "Nonequilibrium Viscous Shock–Layer Flow over Blunt Sphere–Cones at Angle–of–Attack," AIAA Paper No.82–0825,1982.

[3] Davis,R.T., "Numerical Solution of the Hypersonic Viscous Shock Layer Equations," AIAA Journal, Vol.8, No.5, May 1970, pp.843–851.

[4] Moss,J.N., "Reacting Viscous–Shock–Layer Solutions with Multicomponent Diffusion and Mass Injection," NASA TR R–411, June 1974.

[5] Miner,E.W. and Lewis,C.H., "Viscous Shock–Layer Flow for the Space Shuttle Windward Plane of Symmetry," AIAA Journal, Vol.14, No.1, 1976

[6] Cheng,H.K., "The Blunt–Body Problem in Hypersonic Flow at Low Reynolds Number," IAS Paper No.63–92, Jan. 1963.

[7] Browne,W.G., "Thermodynamic Properties of Some Diatoms and Diatomic Ions at High Temperature," MSD Advanced Aerospace Physics TM8, General Electric Co., Philadelphia, Pa., May 1962.

[8] Browne, W.G., "Thermodynamic Properties of Some Atoms and Atomic Ions," MSD Engineering Physics TM2, General Electric Co. Philadelphia, Pa., 1962.

[9] Blottner,F.G.,Johnson,Margaret and Ellis, Molly, "Chemically Reacting Viscous Flow Program for Multi–Component Gas Mixtures," Sandia Laboratories Report SC–RR–70–754, Dec. 1971.

[10] Shen Jianwei and Qu Zhanghua, "Numerical Calculation of Hypersonic Noneqilibrium

Viscous Shock–Layer Flow over a Slender Body with Blunt Nose," Journal of Chinese Society of Astronautics, No.3, 1988
[11] Engle, C.D. and Farmer, R.C., "Ablation and Radiation Coupled Viscous Hypersonic Shock Layer," NASA Grant NGR 19–001059, 1971
[12] Gupta,R.N., "Navier–Stokes and Viscous Shock–Layer Solutions for Radiating Hypersonic Flows," AIAA Paper No.87–1576, 1987.
[13] Moss,J.N. and Bird,G.A.," Nonequilibrium Thermal Radiation for an Aeroassist Flight Experiment Vehicle," AIAA Paper No.88–0081, 1988.
[14] Caochon, D.L., "Radiative Heating Results from The Fire II Flight Experiment at a Reentry Velocity of 11.4 Kilometers Per Second," NASA TM X–1402, 1966.
[15] Wilson,K.H.,"Stagnation Point Analysis of Coupled Viscous Radiating Flow with Massive Blowing", NASA CR–1548, 1971.

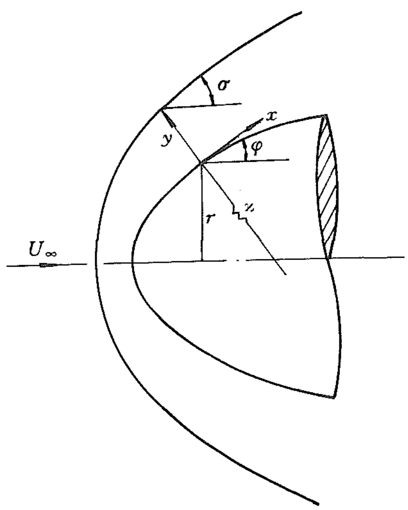

Fig.1 Body oriented coordinate system

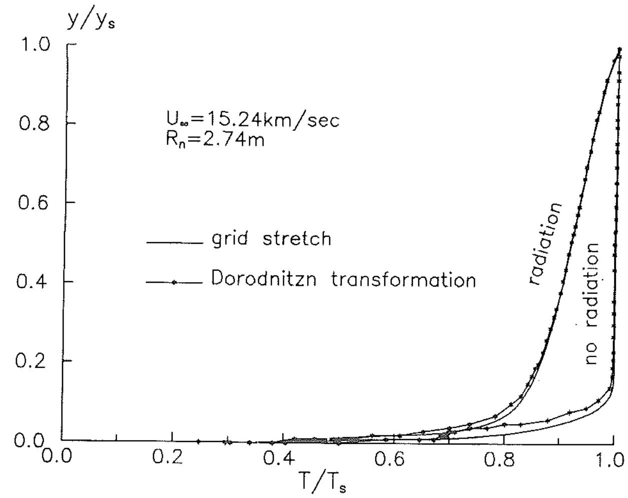

Fig.3 Temperature profiles for radiation and no radiation

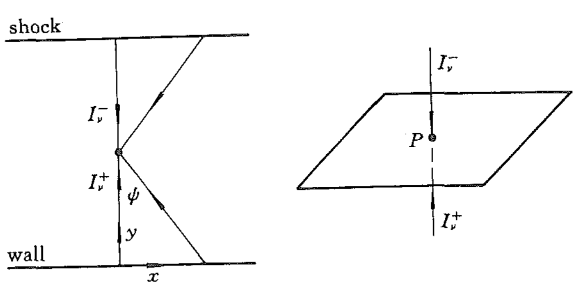

Fig.2 One–dimensional planar medium for radiative transfer

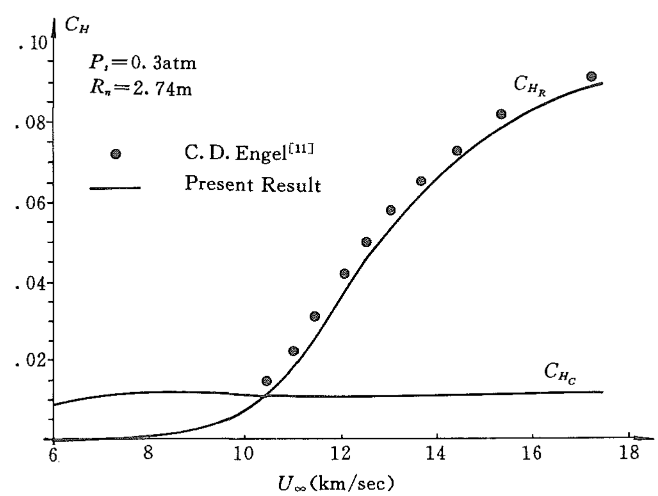

Fig.4 Surface heating transfer coefficient for different freestream velocity

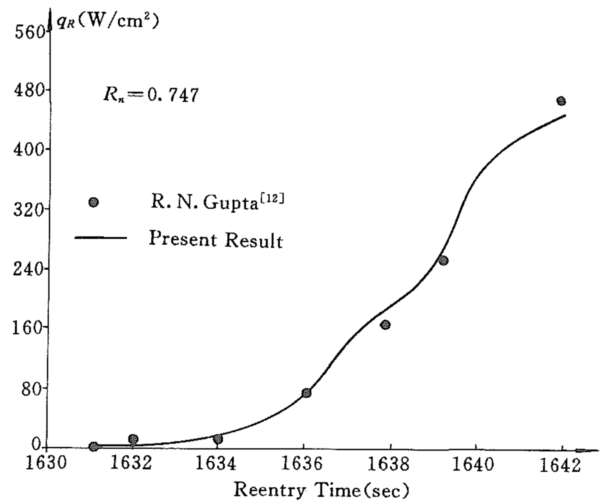

Fig.5 Radiative heating rate at the stagnation streamline

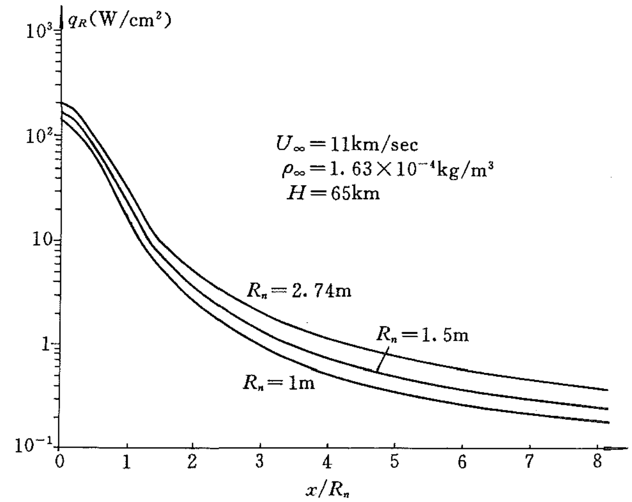

Fig.8 Radiative heating transfer distribution for different nose radius

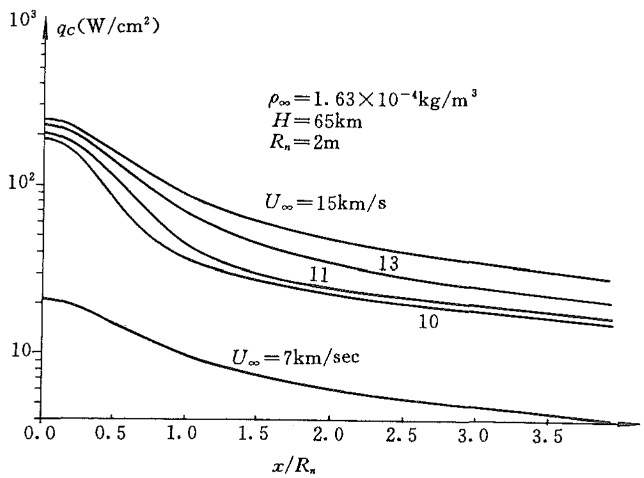

Fig.6 Convective heating transfer distribution for different reentry velocity

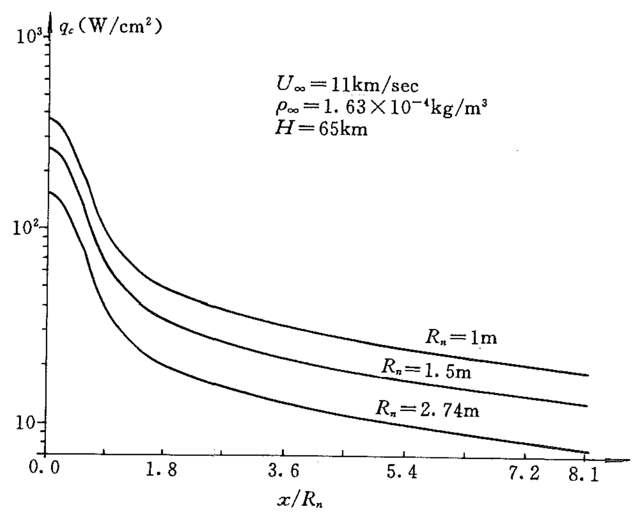

Fig.9 Convective heating transfer distribution for different nose radius

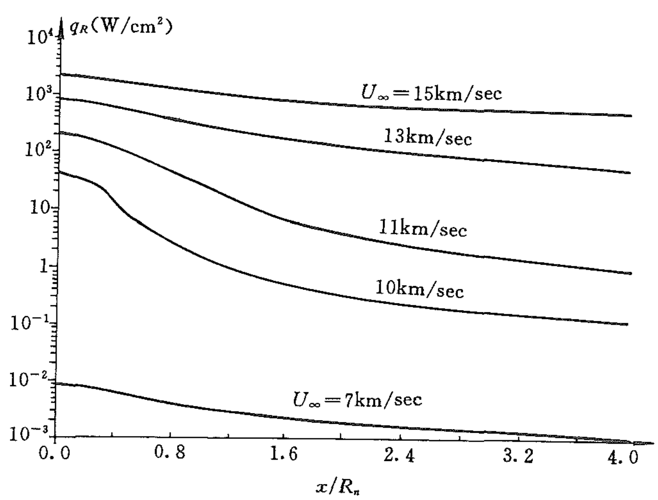

Fig.7 radiative heating transfer distribution for different reentry velocity

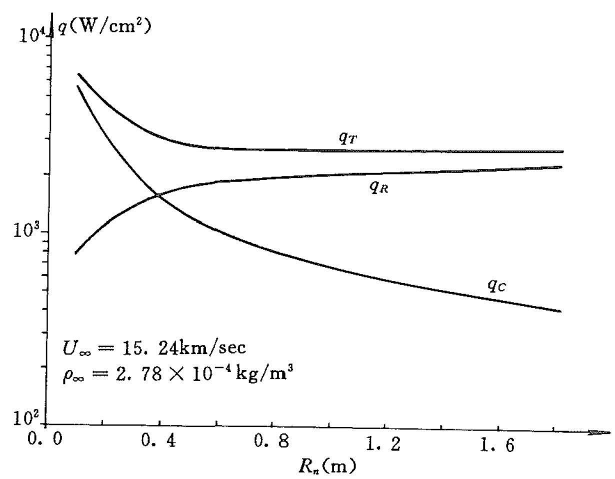

Fig.10 Change of surface heating transfer rate with nose radius

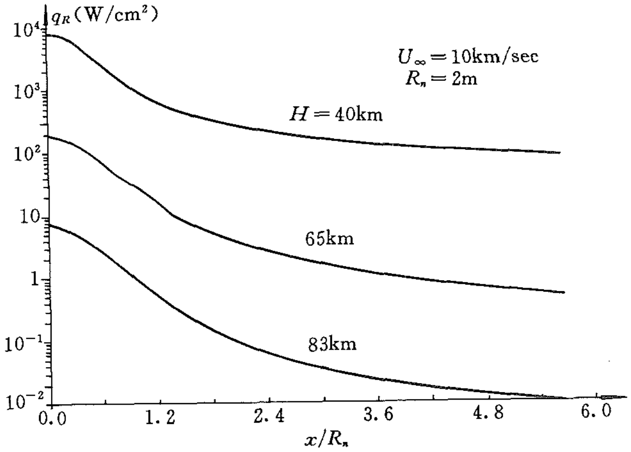

Fig.11 Radiative heating transfer at different altitude

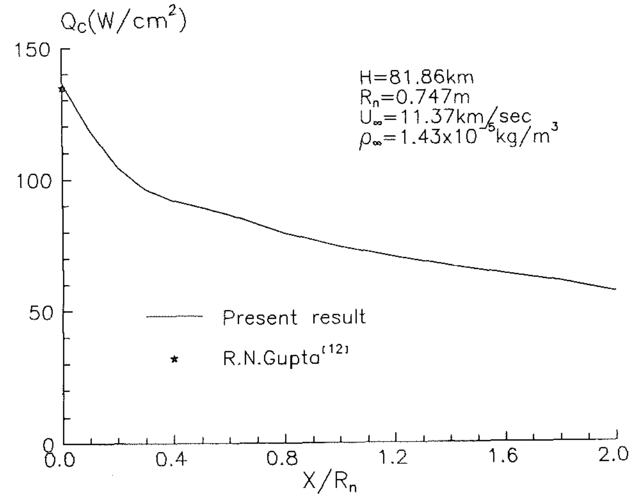

Fig.14 Convective heating transfer distribution at the altitude of 81.86km

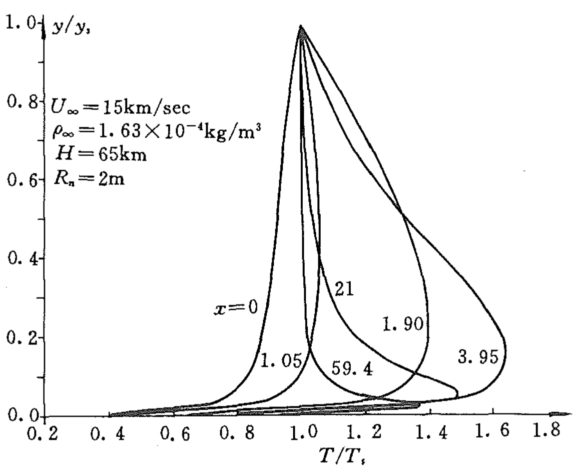

Fig.12 Temperature profiles at different station along the body

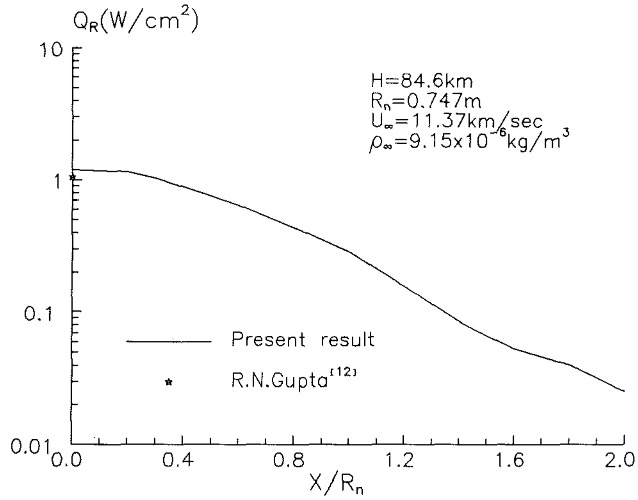

Fig.15 Radiative heating transfer distribution at the altitude of 84.60km

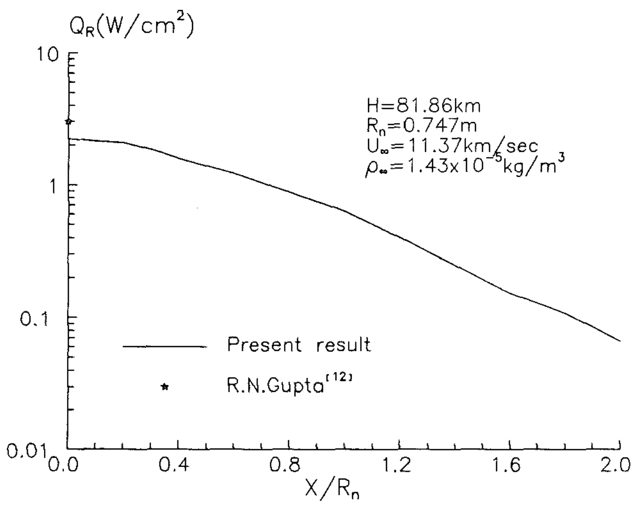

Fig.13 Radiative heating transfer distribution at the altitude of 81.86km

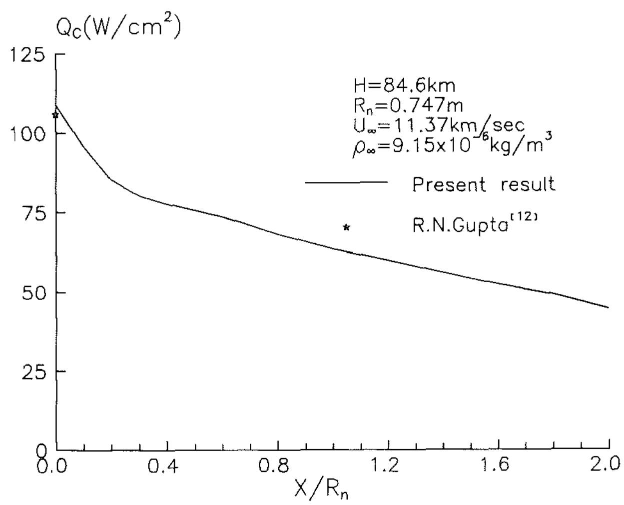

Fig.16 Convective heating transfer distribution at the altitude of 84.60km

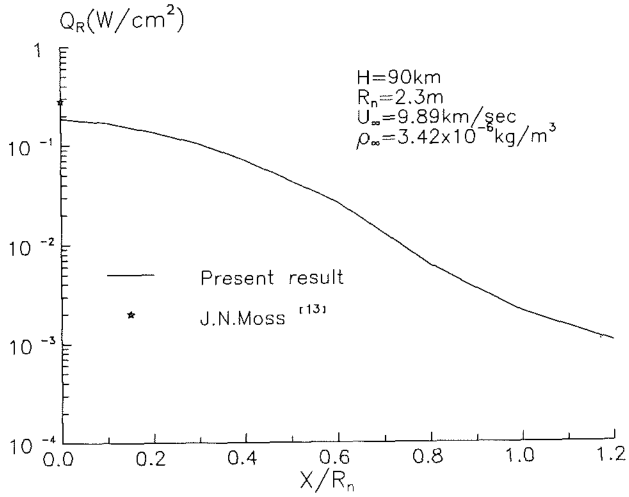

Fig.17 Radiative heating transfer distribution at the altitude of 90km

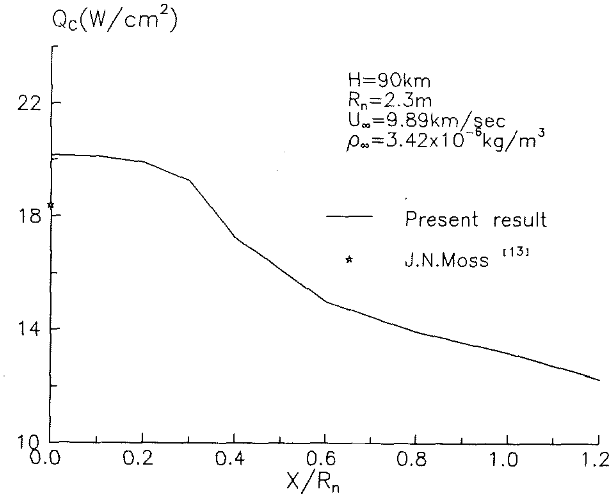

Fig.18 Convective heating transfer distribution at the altitude of 90km